



## A new mesoscopic scale timestep adjustable non-dimensional lattice Boltzmann method for melting and solidification heat transfer

Yan Su <sup>a,\*</sup>, Jane H. Davidson <sup>b</sup>

<sup>a</sup> Department of Electromechanical Engineering, FST, University of Macau, Taipa, Macau

<sup>b</sup> Department of Mechanical Engineering, University of Minnesota, Minneapolis, MN 55455, USA



### ARTICLE INFO

#### Article history:

Received 15 June 2015

Received in revised form 23 September 2015

Accepted 25 September 2015

#### Keywords:

Melting

Non-dimensional lattice Boltzmann method

Phase change

Solidification

### ABSTRACT

A mesoscopic scale timestep adjustable non-dimensional lattice Boltzmann method (NDLBM) for fluid flow and heat transfer with solid–liquid phase change is developed using a scaling analysis based on the mesoscopic length and velocity scales. The interface between fluid and solid is treated as a mixture domain with transient porosity distributions and thickness. Timesteps are adjusted by using a transient mesoscopic Mach number independent of mesh size to speed up the computation. The code is validated by comparison of transient Nusselt numbers, isotherms, streamlines, and porosity with prior studies of natural convection in a square enclosure with and without phase change material. A benchmark problem is proposed to obtain the same equilibrium state for both melting and solidification procedures. Full maps of the flow and heat transfer patterns for both melting and solidification are presented based on the key dimensionless governing parameters. The effects of Mach, Stefan (0.01–10), Rayleigh ( $10^3$ – $10^8$ ), and Prandtl (0.1–10) numbers are discussed.

© 2015 Elsevier Ltd. All rights reserved.

### 1. Introduction

Heat transfer with solid–liquid phase change has wide engineering application such as casting, material processes, and energy storage [1,2]. Two challenging problems in the simulations of transient fluid flow and heat transfer during melting and solidification are the evolving nature of the fluid–solid interface [3,4], and the multiple length and time scales [5,6]. Recently the lattice Boltzmann method (LBM) was proposed to increase computational speed compared to conventional finite difference, finite element, and control volume methods [7–13]. To model the latent heat of melting, an extra source term is introduced in the energy equation [1,14,15]. One limitation of previous LBM studies of phase change is treatment of the moving interface between solid and liquid. The no-slip velocity condition on the moving interface was modeled by an immersed moving boundary scheme, which assumes the interface between fluid and solid domains is an infinitely thin boundary [14,16]. This approach does not capture the true nature of the interface which is a mixture zone filled with both solid and liquid.

To address this issue, we develop a mesoscopic scale timestep adjustable non-dimensional lattice Boltzmann method (NDLBM) for melting and solidification heat transfer and introduce the

concept of porosity to describe the transient fluid component ratio in each mesoscopic element. This approach is thus able to model the mixture zone at the interface between phases. The porosity in the mixture zone varies from 1 to 0 from pure fluid to pure solid, respectively.

Different from the fixed time step mesoscopic length and macroscopic velocity scale based NDLBM of Su et al. [17,18], the present mesoscopic length and mesoscopic velocity scale based NDLBM makes it possible to adjust the timesteps in time by using a transient mesoscopic Mach number that is independent of mesh size. According to the transient heat transfer characteristics, an exponential time increasing function for mesoscopic Mach number is applied to speed up the simulations while maintaining high accuracy. This approach makes it possible to simulate cases with macroscopic Rayleigh numbers up to  $10^8$  in reasonable computational time. The effects of the dimensionless governing parameters ( $0.01 \leq Ste \leq 10$ ,  $0.1 \leq Pr \leq 10$ , and  $10^3 \leq Ra_L \leq 10^8$ ) on interface, temperature, and flow patterns for both melting and solidification of PCM are presented.

### 2. Governing equations and the non-dimensional lattice Boltzmann method

Sketches of a uniform model for simulation of both solidification and melting for a square enclosure filled with PCM are shown

\* Corresponding author.

E-mail address: [yansu@umac.mo](mailto:yansu@umac.mo) (Y. Su).

## Nomenclature

$c_p$	specific heat capacity, J/kg K
$c_s$	lattice speed of sound, m/s
$c$	mesoscopic velocity scale, m/s
$\mathbf{c}$	mesoscopic velocity vector, m/s
$\mathbf{e}_g$	the unit vector in the gravity direction
$\mathbf{e}_v$	the unit vector in the velocity direction
$f$	density distribution function, kg/m <sup>3</sup>
$F$	force term, N/m <sup>3</sup>
$Fo$	Fourier number, ( $= t\alpha/L^2$ )
$g$	temperature distribution function, K
$g$	gravity acceleration, m/s <sup>2</sup>
$k$	thermal conductivity, W/m K
$L$	macroscopic length scale, m
$L_f$	latent heat per unit mass, J/kg
$H$	height of the enclosure, m
$Ma$	Mach number
$Nu$	Nusselt number
$p$	pressure, N/m <sup>2</sup>
$Pe$	Peclet number
$Pr$	Prandtl number
$Q$	heat source, W/m <sup>3</sup>
$Ra$	Rayleigh number
$Re$	Reynolds number
$Ri$	Richardson number
$Ste$	Stefan number
$t$	time, s
$T$	temperature, K
$\mathbf{v}$	velocity vector, m/s
$U$	macroscopic velocity scale, m/s
$w$	weighting factor
$x, y$	coordinates

### Greek symbols

$\Delta T$	temperature scale, K
------------	----------------------

$\Delta t$	time scale, s
$\Delta x$	lattice size in $x$ direction, m
$\Delta y$	lattice size in $y$ direction, m
$\alpha$	thermal diffusivity, m <sup>2</sup> /s
$\beta$	thermal expansion coefficient
$\zeta$	dimensionless equilibrium function
$\mu$	dynamic viscosity, kg/m s
$\nu$	kinematic viscosity, m <sup>2</sup> /s
$\rho$	density, kg/m <sup>3</sup>
$\tau$	relaxation time, s
$\phi$	porosity
$\ell$	mesoscopic length scale, m

### Subscripts

$c$	mesoscopic velocity scale
$equ$	equilibrium state
$f$	fluid
$high$	higher value
$k$	the index of the 9 directions
$m$	mixture of solid and liquid PCM
$od$	opposite direction
$low$	lower value
$L$	macroscopic length scale
$ref$	reference
$s$	solid
$U$	macroscopic velocity scale
$w$	wall
$\ell$	mesoscopic length scale
$0$	initial time value

### Superscripts

*	dimensionless variables
---	-------------------------

in Fig. 1. The procedure from (a) to (b) is a solidification procedure, and the procedure from (c) to (b) is a melting procedure. The boundary conditions for both solidification and melting are identical. The left hand side is a hot wall with a constant temperature  $T_{high}$ , and the right hand side is a cold wall with a constant temperature  $T_{low}$ . The melting/solidification temperature is the average of  $T_{high}$  and  $T_{low}$ . Both top and bottom walls are adiabatic. The initial velocity is  $\mathbf{v}_0 = 0$  and the initial temperature is  $T_0 = T_m$ . Note that the present initial condition for temperature is different from almost all previous studies on natural convection solid/liquid phase change in a square cavity, which have either subcooling [6,14,19] or subheating [20] initial conditions, i.e. their initial temperature equals  $T_{low}$  for melting and  $T_{high}$  for solidification. In the present benchmark problem, the only difference between melting and solidification is the initial porosity. For solidification  $\phi_0 = 1$ , representing the liquid phase, while for melting  $\phi_0 = 0$ , representing the solid phase. The model guarantees that both melting and solidification procedures reach the same equilibrium state. Also the phase change starts from the initial time.

### 2.1. Governing equations

For natural convection of a Newtonian incompressible fluid with solid–liquid phase change, the microscopic continuity equation is,

$$\nabla \cdot \mathbf{v}_f = 0. \quad (1)$$

The microscopic momentum equation for natural convection flow under the Boussinesq assumption, is,

$$\rho_f \left[ \frac{\partial \mathbf{v}_f}{\partial t} + \nabla \cdot (\mathbf{v}_f \mathbf{v}_f) \right] = -\nabla p_f + \mu_f \nabla^2 \mathbf{v}_f + \rho_f g \beta (T_f - T_{ref}) (-\mathbf{e}_g \cdot \mathbf{e}_v), \quad (2)$$

The microscopic energy equations for the fluid and solid phases are,

$$(\rho C_p)_f \left[ \frac{\partial T_f}{\partial t} + \nabla \cdot (\mathbf{v}_f T_f) \right] = \nabla \cdot (k_f \nabla T_f) + q_{L_f} + q_{sf} \quad (3)$$

and

$$(\rho C_p)_s \frac{\partial T_s}{\partial t} = \nabla \cdot (k_s \nabla T_s) + q_{L_f} - q_{sf}, \quad (4)$$

respectively, where  $q_{sf}$  is the heat transferred from solid to liquid, and  $q_{L_f}$  is the latent heat of solid–liquid phase change. The latent heat  $q_{L_f}$  is defined as,

$$q_{L_f} = -\frac{\partial \rho L_f \phi}{\partial t}, \quad (5)$$

where  $L_f$  is latent heat per unit mass, and the porosity  $\phi$  is defined as the fraction of the volume of the fluid phase,

$$\phi = \frac{V_f}{V_s + V_f}. \quad (6)$$

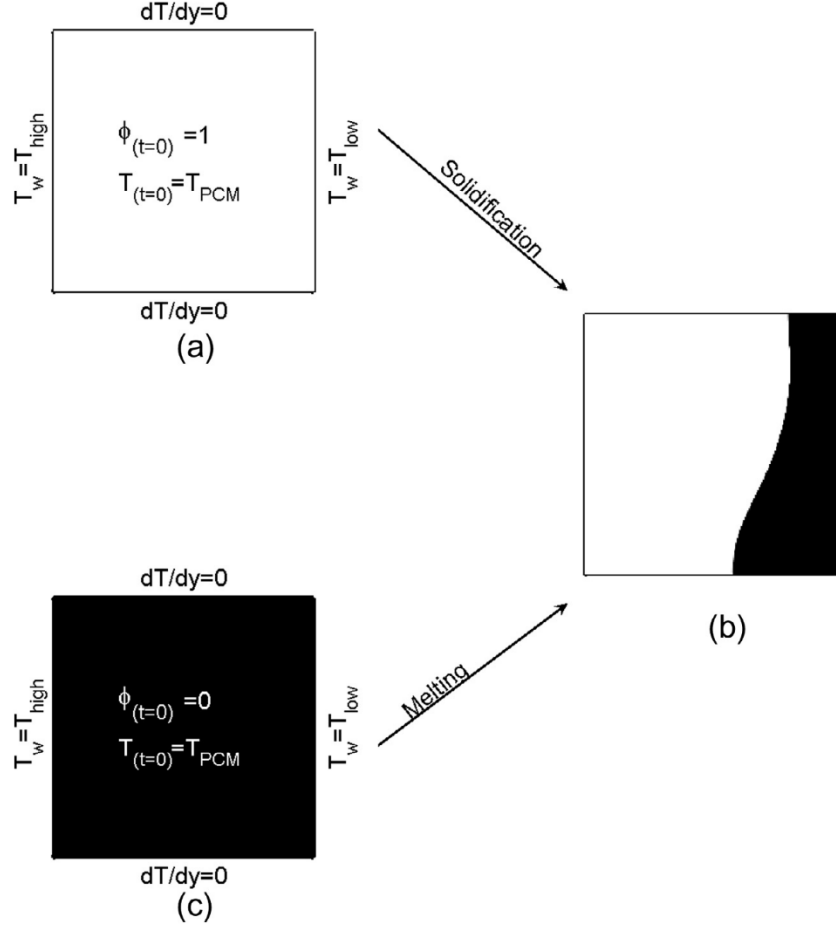


**Fig. 1.** Sketch of the uniform model for simulation of solidification (a) and melting (c) for an enclosure filled with PCM.

Porosity  $\phi$  is a function of space and time. Because of the small range of temperature change in the mixture of solid and fluid during phase change, the local thermal equilibrium is applied. Combining Eqs. (3) and (4) based on the porosity  $\phi$  in Eq. (6), the energy equation is expressed as,

$$\begin{aligned} & [\phi(\rho C_p)_f + (1 - \phi)(\rho C_p)_s] \left[ \frac{\partial T}{\partial t} + \nabla \cdot (\phi \mathbf{v}_f T) \right] \\ & = [\phi k_f + (1 - \phi)k_s] \nabla^2 T - [\phi(\rho L_f)_f + (1 - \phi)(\rho L_f)_s] \frac{\partial \phi}{\partial t}. \end{aligned} \quad (7)$$

Effective transport parameters for the mixture of fluid and solid are expressed in terms of the porosity  $\phi$ . The effective density, thermal capacity, and thermal diffusivity are defined by Eqs. (8)–(10) as,

$$\rho_m = \phi \rho_f + (1 - \phi) \rho_s, \quad (8)$$

$$c_{pm} = \frac{(\rho c_p)_m}{\rho_m} = \frac{\phi(\rho c_p)_f + (1 - \phi)(\rho c_p)_s}{\phi \rho_f + (1 - \phi) \rho_s} \quad (9)$$

and

$$\alpha_m = \frac{\phi k_f + (1 - \phi)k_s}{\phi(\rho C_p)_f + (1 - \phi)(\rho C_p)_s}. \quad (10)$$

Note that if the PCM melts over a temperature range  $\delta T_m$ ,  $\delta T_m = T_{m_{high}} - T_{m_{low}}$ . In this case, Eq. (9) should be replaced by  $c_{pm} = L_f/\delta T_m$  for the mixture zone with  $0 < \phi < 1$ . Using those effective properties and assuming  $L_f$  is a constant, the microscopic

momentum and energy equations for the solid–liquid phase change can be rewritten in simplified form as,

$$\frac{\partial \mathbf{v}}{\partial t} + \nabla \cdot (\mathbf{v} \mathbf{v}) = -\frac{1}{\rho_f} \nabla p_f + v_f \nabla^2 \mathbf{v} + g \beta(T - T_{ref})(-\mathbf{e}_g \cdot \mathbf{e}_v) \quad (11)$$

and

$$\frac{\partial T}{\partial t} + \nabla \cdot (\phi \mathbf{v} T) = \alpha_m \nabla^2 T - \left( \frac{L_f}{c_{pm}} \right) \frac{\partial \phi}{\partial t}, \quad (12)$$

respectively.

## 2.2. Dimensionless macroscopic equations and governing parameters

The dimensionless macroscopic momentum and energy equation are obtained from Eqs. (11) and (12) by a scaling analysis based on the macroscopic length scale  $L$ , velocity scale  $U$ , and time scale  $L/U$ :

$$\frac{\partial^* \mathbf{v}^*}{\partial^* t^*} + \nabla^* \cdot (\mathbf{v}^* \mathbf{v}^*) = -\nabla^* p_f^* + \frac{1}{Re_{U,L}} \nabla^{*2} \mathbf{v}^* + Ri_{U,L} T^* (-\mathbf{e}_g \cdot \mathbf{e}_{v^*}) \quad (13)$$

and

$$\frac{\partial^* T^*}{\partial^* t^*} + \nabla^* \cdot (\phi \mathbf{v}^* T^*) = \frac{1}{Pe_{U,L}} \nabla^{*2} T^* - \frac{1}{Ste} \left( \frac{c_{pf}}{c_{pm}} \right) \frac{\partial^* \phi}{\partial^* t^*}, \quad (14)$$

where  $Re_{U,L}$  is the macroscopic Reynolds number,

$$Re_{U,L} = \frac{UL}{v_f} = \frac{L \sqrt{g \beta \Delta T L}}{v_f} \quad (15)$$

and  $Pe_{U,L}$  is the macroscopic Peclet number,

$$Pe_{U,L} = Re_{U,L} Pr_m. \quad (16)$$

$Pr_m$  is given by,

$$Pr_m = \begin{cases} Pr_f = \frac{v_f}{\alpha_f}, & \text{for pure fluid } \phi = 1, \\ Pr_s = Pr_f \left( \frac{\alpha_f}{\alpha_s} \right), & \text{for pure solid } \phi = 0, \\ Pr_f \phi + Pr_s (1 - \phi), & \text{for fluid solid mixture } 0 < \phi < 1. \end{cases} \quad (17)$$

The Stefan number is defined as,

$$Ste = \frac{L_f}{c_{pf} \Delta T}. \quad (18)$$

Hence the macroscopic Richardson number is expressed as,

$$Ri_{U,L} = \frac{g \beta \Delta T L}{U^2}. \quad (19)$$

The corresponding macroscopic Rayleigh number for natural convection is

$$Ra_L = \frac{g \beta \Delta T L^3}{v_f \alpha_f} = Re_{U,L}^2 Pr_f Ri_{U,L}, \quad (20)$$

where  $U = \sqrt{g \beta \Delta T L}$  and  $Ri_{U,L} = 1$ .

### 2.3. Dimensionless mesoscopic equations and governing parameters

Similar to the above macroscopic scaling analysis, if we use the mesoscopic length scale,  $\ell = \Delta x$ , mesoscopic velocity scale  $c = c_s/c_s^*$  ( $c_s$  is the mesoscopic sound speed, and  $c_s^*$  is the dimensionless mesoscopic sound speed), and mesoscopic time scale  $\Delta t = \ell/c$  to scale Eqs. (11) and (12), we obtain the mesoscopic dimensionless momentum and energy equations:

$$\frac{\partial^* \mathbf{v}^*}{\partial^* t^*} + \nabla^* \cdot (\mathbf{v}^* \mathbf{v}^*) = -\nabla^* p_f^* + \frac{1}{Re_{c,\ell}} \nabla^{*2} \mathbf{v}^* + Ri_{c,\ell} T^* (-\mathbf{e}_g \cdot \mathbf{e}_{\mathbf{v}^*}) \quad (21)$$

and

$$\frac{\partial^* T^*}{\partial^* t^*} + \nabla^* \cdot (\phi \mathbf{v}^* T) = \frac{1}{Pe_{c,\ell}} \nabla^{*2} T - \frac{1}{Ste} \left( \frac{c_{pf}}{c_{pm}} \right) \frac{\partial^* \phi}{\partial^* t^*}. \quad (22)$$

The mesoscopic dimensionless parameters based on the mesoscopic velocity scale  $c$  and the mesoscopic length scale  $\ell$ , are

$$Re_{c,\ell} = \frac{c \ell}{v_f} = \frac{Re_{U,\ell}}{c_s^* Ma_\ell}, \quad (23)$$

$$Pe_{c,\ell} = \frac{Pe_{U,\ell}}{c_s^* Ma_\ell} = \frac{Re_{U,\ell}}{c_s^* Ma_\ell} Pr_m, \quad (24)$$

$$Ri_{c,\ell} = \frac{g \beta \Delta T \ell}{c^2} = (c_s^* Ma_\ell)^2 \frac{\ell}{L} \quad (25)$$

and

$$Ma_\ell = \frac{U}{c_s} = \frac{U}{c_s^* c}. \quad (26)$$

The Reynolds number based the macroscopic velocity scale  $U$  and the mesoscopic length scale  $\ell$  is

$$Re_{U,\ell} = \frac{U \ell}{v_f} = \left( \frac{\ell}{L} \right) Re_{U,L}. \quad (27)$$

The corresponding mesoscopic Rayleigh number is,

$$Ra_\ell = \frac{g \beta \Delta T \ell^3}{v_f \alpha_f} = Re_{c,\ell}^2 Pr_f Ri_{c,\ell}. \quad (28)$$

### 2.4. Non-Dimensional lattice Boltzmann method for dimensionless mesoscopic equations

For the model shown in Fig. 1, the macroscopic length scale is the width or height of the square enclosure, i.e.  $L = H$ . The domain is meshed in size of  $n \times m$ . The lattice mesh size is the mesoscopic length scale,  $\ell = \Delta x = \Delta y = H/m = L/n$ . The temperature scale is the temperature difference between the hot wall and the reference temperature, i.e.  $\Delta T = T_{high} - T_{ref}$ , where  $T_{ref}$  is the reference temperature for computation. The macroscopic velocity scale for the natural convection is  $U = \sqrt{g \beta \Delta T H}$ , and the mesoscopic velocity scale is lattice velocity  $c$ .

A NDLBM corresponding to the dimensionless mesoscopic Eqs. (21) and (22) is developed to solve the problem. Different from the previous NDLBM based on the mesoscopic length scale and the macroscopic velocity scale [17,18], which uses fixed time steps, the present NDLBM is based on the mesoscopic length scale and the mesoscopic velocity scale. Hence the present NDLBM makes it possible to change the time step by introducing the transient  $Ma_\ell$ , which changes  $dt$  without changing mesh size  $\ell$ . The D2Q9 scheme is chosen in the present study because previous studies show that two-dimensional simulations can capture the heat transfer coefficient as well as three dimensional simulations, although fluid patterns may change from spirals to recirculations [21].

We denote  $f^*$  as the dimensionless density distribution function and  $g^*$  as the dimensionless temperature distribution function. Using the mesoscopic length scale  $\ell = \Delta x$ , velocity scale  $c$ , time scale  $\Delta t = \ell/c$ , temperature scale  $\Delta T = T_{high} - T_{ref}$ , and density scale  $\rho_{f_0}$ , we obtain the following discrete dimensionless equations for momentum equation and energy equation respectively:

$$f_k^*(\mathbf{x}^* + \mathbf{c}_k^*, t^* + 1) = f_k^*(\mathbf{x}^*, t^*) - \frac{1}{\tau_f^*} (f_k^*(\mathbf{x}^*, t^*) - f_k^{eq*}(\mathbf{x}^*, t^*)) + F_k^*, \quad (29)$$

$$g_k^*(\mathbf{x}^* + \mathbf{c}_k^*, t^* + 1) = g_k^*(\mathbf{x}^*, t^*) - \frac{1}{\tau_g^*} (g_k^*(\mathbf{x}^*, t^*) - g_k^{eq*}(\mathbf{x}^*, t^*)) + Q_k^*. \quad (30)$$

Then, the respective dimensionless density, velocity, and temperature are as follows:

$$\rho^* = \sum_k f_k^*, \quad (31)$$

$$\mathbf{v}^* = \phi \sum_k f_k^* \mathbf{c}_k^* \Big/ \sum_k f_k^*, \quad (32)$$

$$T^* = \sum_k g_k^*. \quad (33)$$

The local equilibrium distribution functions for fluid flow and heat transfer are given by,

$$f_k^{eq*} = w_{k\zeta}(\mathbf{c}_k^*, \mathbf{v}^*) \rho^* \quad (34)$$

and

$$g_k^{eq*} = w_{k\zeta}(\mathbf{c}_k^*, \mathbf{v}^*) T^*, \quad (35)$$

respectively, where  $\zeta(\mathbf{c}_k^*, \mathbf{v}^*)$  is obtained based on the Bhatnagar-Gross-Krook (BGK) model [11] as,

$$\zeta(\mathbf{c}_k^*, \mathbf{v}^*) = \left[ 1 + \left( \frac{\mathbf{c}_k^* \cdot \mathbf{v}^*}{c_s^2} \right) + \frac{1}{2} \left( \frac{\mathbf{c}_k^* \cdot \mathbf{v}^*}{c_s^2} \right)^2 - \frac{1}{2} \left( \frac{\mathbf{v}^* \cdot \mathbf{v}^*}{c_s^2} \right) \right]. \quad (36)$$

For the D2Q9 lattice mesh, the dimensionless speed of sound is  $c_s^* = 1/\sqrt{3}$ , according to  $c_s^2 = c^2/3$  [22]. The corresponding dimensionless discrete velocities are,

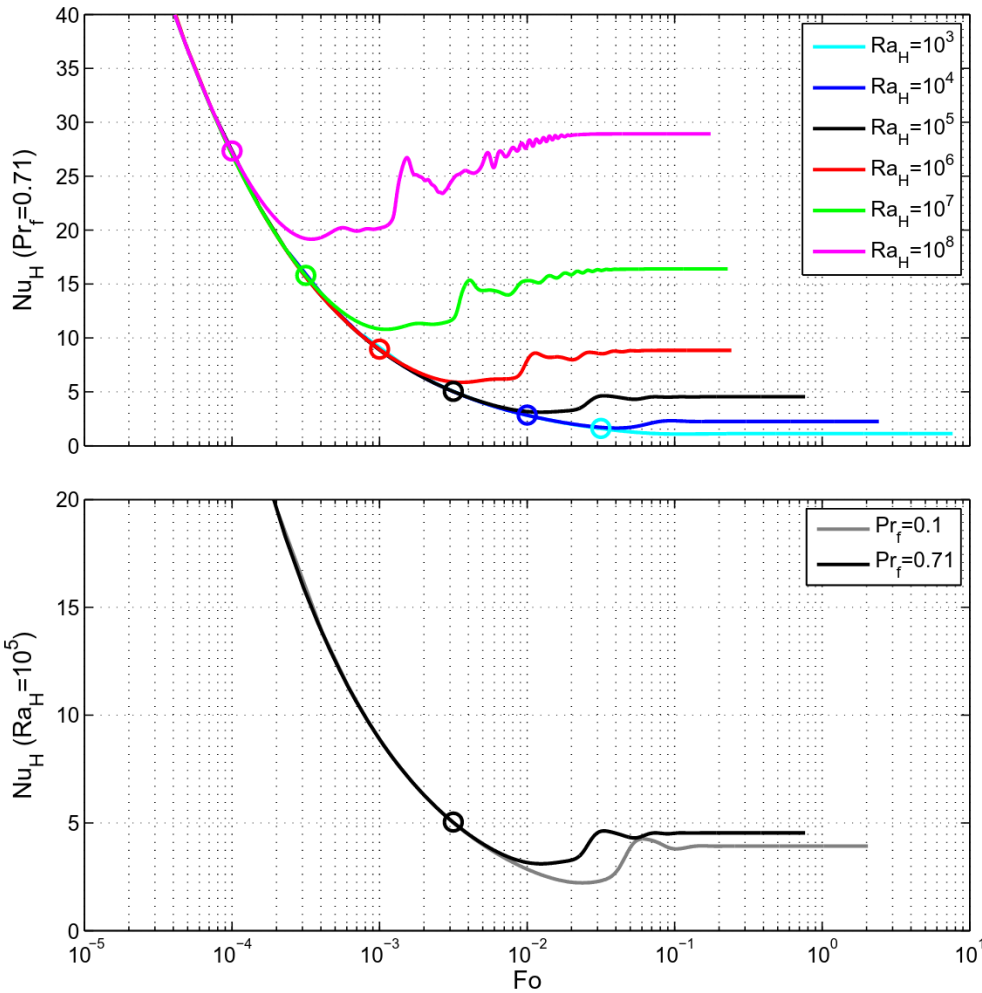


**Fig. 2.** Transient Nusselt numbers for pure natural convection in a square enclosure.

**Table 1**  
Comparison of pure natural convection in a square enclosure.

	$Pr_f$	$Ra_L$	$Nu_H$
SIMPLE method [29]	0.1	$1 \times 10^5$	3.9248
Projection method [2]	0.1	$1 \times 10^5$	3.9250
Present NDLBM	0.1	$1 \times 10^5$	3.9253
De Vahl Davis [28]	0.71	$1 \times 10^4$	2.238
Fuentes [30]	0.71	$1 \times 10^4$	2.239
Present NDLBM	0.71	$1 \times 10^4$	2.2494
De Vahl Davis [28]	0.71	$1 \times 10^5$	4.509
Fuentes [30]	0.71	$1 \times 10^5$	4.510
Present NDLBM	0.71	$1 \times 10^5$	4.5360
De Vahl Davis [28]	0.71	$1 \times 10^6$	8.817
Fuentes [30]	0.71	$1 \times 10^6$	8.828
Present NDLBM	0.71	$1 \times 10^6$	8.8394

Based on the Chapman–Enskog expansion of the mesoscopic dimensionless momentum and energy Eqs. (21) and (22), the dimensionless relaxation times for the flow,  $\tau_f^*$ , and heat transfer,  $\tau_g^*$ , based on the mesoscopic Reynolds number  $Re_{c,\ell}$  and Peclet number  $Pe_{c,\ell}$  are,

$$\tau_f^* = \frac{1}{c_s^{*2} Re_{c,\ell}} + \frac{1}{2} = \frac{Ma_\ell}{c_s^* Pe_{U,\ell}} + \frac{1}{2} \quad (39)$$

and

$$\tau_g^* = \frac{1}{c_s^{*2} Pe_{c,\ell}} + \frac{1}{2} = \frac{Ma_\ell}{c_s^* Pe_{U,\ell}} + \frac{1}{2}. \quad (40)$$

The time step  $dt$  is set equal to  $\Delta t$  to guarantee the dimensionless time step  $dt^* = 1$ . Then the real time step is,

$$dt = \Delta t = \frac{\ell}{c} = c_s^* Ma_\ell \left( \frac{\ell}{U} \right) = \left( \frac{L^2}{\alpha_f} \right) \left( \frac{\ell}{L} \right) \frac{c_s^* Ma_\ell}{Pr_f Re_{U,L}}. \quad (41)$$

The Fourier number  $Fo = t\alpha_f/L^2$  and the corresponding  $dFo$  is,

$$dFo = \frac{\alpha_f}{L^2} dt = \left( \frac{\ell}{L} \right) \frac{c_s^* Ma_\ell}{Pr_f Re_{U,L}}. \quad (42)$$

The numerical error of the present scheme is proportional to  $dt^{-1}$ , i.e.,  $Ma_\ell^{-1}$  and  $Re_{U,L}$ , which agrees with the analysis of Dellar [23].

and the weighting factors are

$$w_k = \begin{cases} 4/9, & k = 0 \\ 1/9, & k = 1, 2, 3, 4, \\ 1/36, & k = 5, 6, 7, 8 \end{cases} \quad (38)$$

$$\mathbf{c}_k^* = \begin{cases} (0, 0), & k = 0 \\ (\pm 1, 0), & k = 1, 2, 3, 4, \\ (\pm 1, \pm 1), & k = 5, 6, 7, 8 \end{cases} \quad (37)$$

An exponential time increasing function shown in Eq. (43) is applied to speed up the computation, according to the transient heat transfer characteristics inside enclosures [24],

$$Ma_\ell = Ma_0 \exp \left[ \frac{t^*}{Pr_f^{1/2} Ra_L^{1/4} (\ell_e)^2} \right]. \quad (43)$$

Also to guarantee the accuracy and reasonable computational speed, the initial time Mach number  $Ma_0$  is selected to be less than or equal to  $\sqrt{\ell/L}$ .

The dimensionless heat source due to phase change is defined as,

$$Q_k^* = -w_k \frac{1}{Ste} \left( \frac{c_{pf}}{c_{pm}} \right) \left( \frac{\partial^* \phi}{\partial t^*} \right). \quad (44)$$

Hence  $Q_k^*$  is negative for melting and positive for solidification.

The dimensionless force term due to buoyancy is,

$$F_k^* = w_k \left( \frac{-\mathbf{e}_g \cdot \mathbf{c}_k^*}{c_s^{*2}} \right) Ri_{c,\ell} \phi T^*, \quad (45)$$

where  $Ri_{c,\ell}$  is the mesoscopic Richardson number defined in Eq. (25).

Similar to LBM with units [25,26], the bounce back boundary conditions in dimensionless form are applied as no slip zero velocity conditions for the walls,

$$f_k^* = f_{k_{od}}^*, \quad k = 0-8, \quad (46)$$

where  $k_{od}$  is the opposite direction of  $k$ . According to boundary conditions with units [27], the dimensionless temperature boundary conditions at the left and right walls are,

$$g_k^* = T_w^* (w_k + w_{k_{od}}) - g_{k_{od}}^*, \quad (47)$$

where  $T_w = T_{high}^*$  and  $T_w = T_{low}^*$  are the left and right vertical wall temperature boundary conditions. For the bottom and top adiabatic walls, zero heat flux boundary conditions are assumed,

$$g_{k,w}^* = g_{k,w-1}^*. \quad (48)$$

where,  $w-1$  is the mesh layer nearest to the wall.

Zero initial velocity and uniform initial temperature are specified for flow and heat transfer fields. The corresponding equilibrium distribution functions for  $f^*$  and  $g^*$  are,

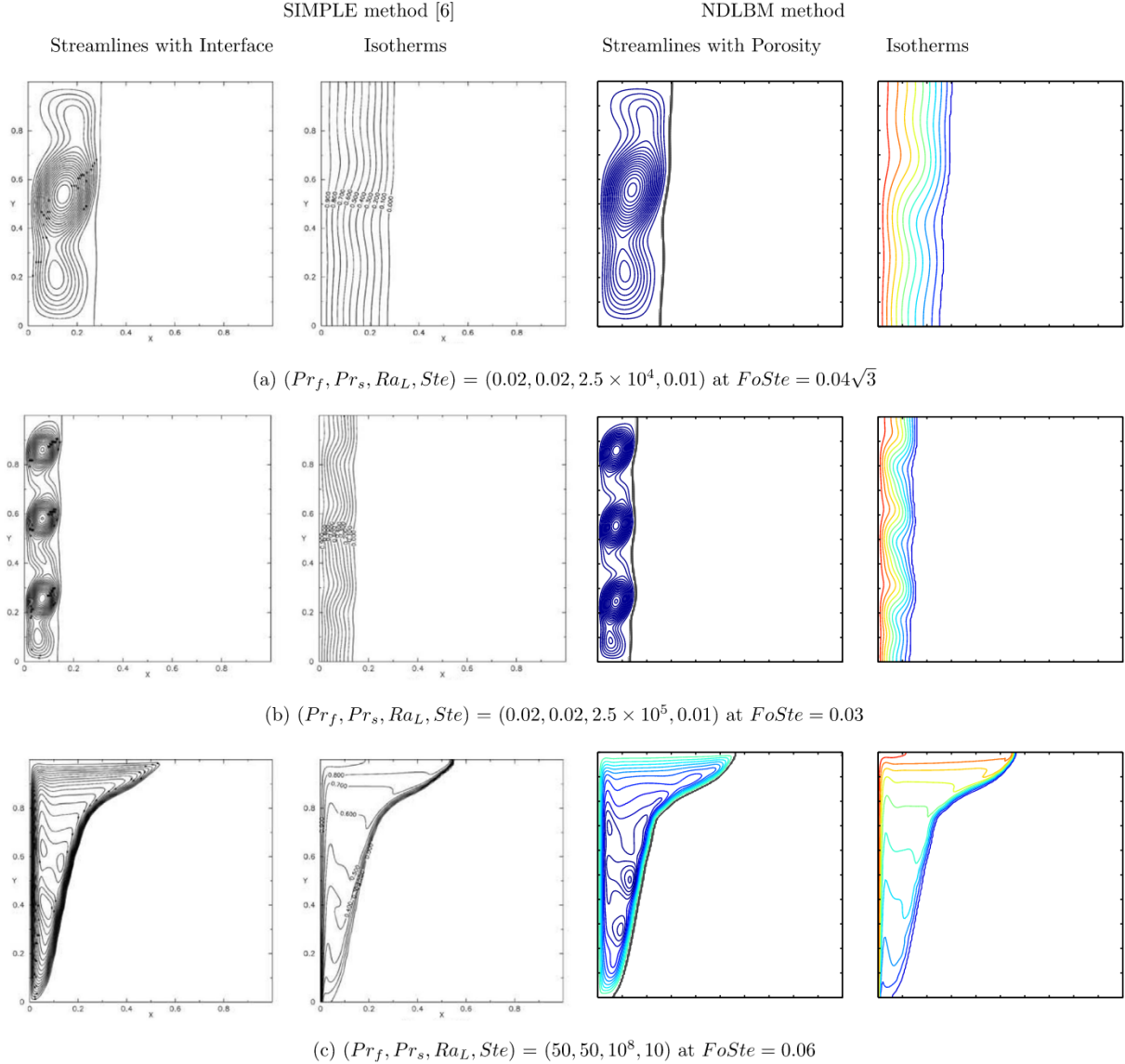


**Fig. 3.** Comparison of transient streamlines with porosity and isotherms of the NDLM and the adaptive grid SIMPLE method of Mencinger [6].

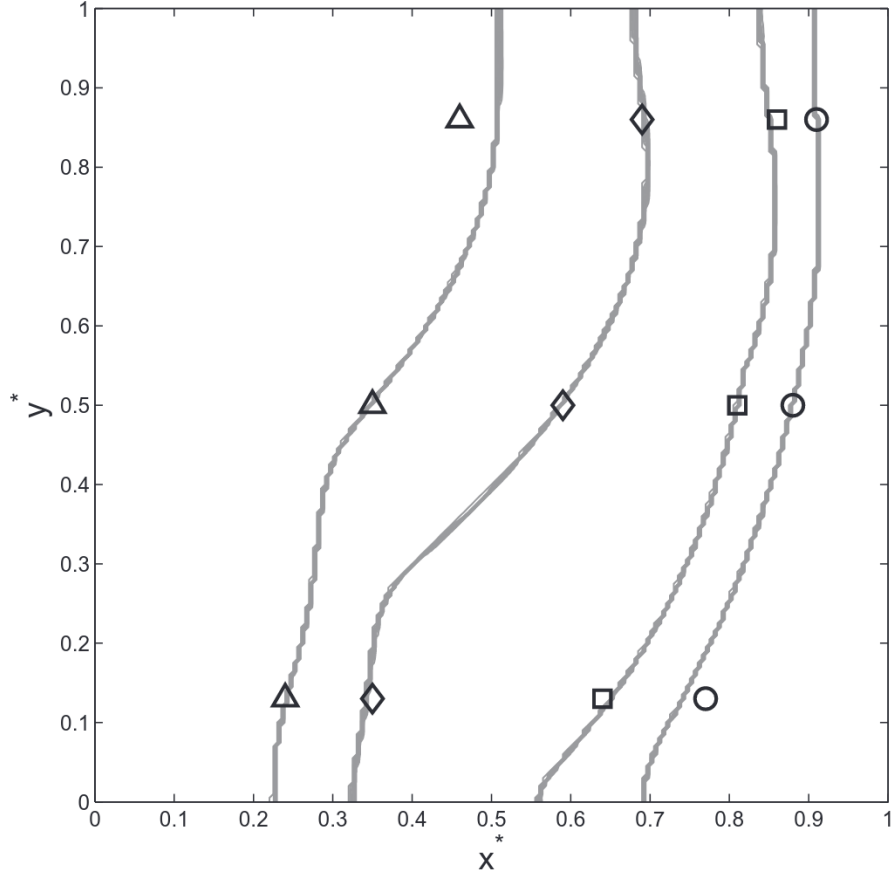


**Fig. 4.** Comparison of the equilibrium state melting zone positions with the experimental study of Bechermann and Viskanta [19]: the black circles, diamonds, triangles, and squares represent the experimental results of  $(Ra_L, Ste, T_{PCM}^*) = (3.275 \times 10^5, 5.074 \times 10^{-2}, -0.36)$ ,  $(3.275 \times 10^5, 5.074 \times 10^{-2}, +0.32)$ ,  $(1.673 \times 10^5, 2.592 \times 10^{-2}, +0.48)$ , and  $(4.877 \times 10^5, 7.557 \times 10^{-2}, -0.0133)$ , respectively. Solid gray lines represent melting zone positions obtained by the present NDLBM code.

$$f_k^* = w_k \rho_0^*, \quad \text{at } t^* = 0 \quad (49)$$

and

$$g_k^* = w_k T_0^*, \quad \text{at } t^* = 0. \quad (50)$$

For both the melting and solidification procedures, the initial temperature is the phase change temperature i.e.,  $T_0^* = T_m^* = 0$ .

A computational code for the present NDLBM is developed in Fortran 90, and is compiled and run on the high performance computing cluster with GNU/Linux operating system (CentOS 5.5 64-bit). To maintain the accuracy, the mesh size  $n \times m$  is  $200 \times 200$  and results are validated by comparison to previous studies for  $10^3 \leq Ra_L \leq 10^8$ . As we discussed before, in the present NDLBM simulations, we change  $dt$  by changing the mesoscopic Mach number  $Ma_\ell$  shown in Eq. (43). The convergence of the present problem is set to ensure the average porosity change is less than  $10^{-6}$ .

### 3. Results

#### 3.1. Validation

To validate the time step adjustable NDLBM method, we first consider the problem for natural convection in a square enclosure with opposing hot and cold vertical surfaces [28]. The two vertical sides of the square enclosure are given by constant temperature of  $T_{high}$  and  $T_{low}$  respectively. The top and bottom walls of the square enclosure are assumed adiabatic. To solve this problem, we set  $T_{ref} = T_{low}$ , and  $\Delta T = T_{high} - T_{low}$  for Fig. 1(c). Hence  $T_{high}^* = 1$  and

$T_{low}^* = 0$ . The porosity is  $\phi = \phi_0 = 1$  for pure fluid. The transient spatially averaged Nusselt number along the hot vertical wall is given in Fig. 2. The solid lines represent the present NDLBM for Rayleigh numbers from  $10^3$  to  $10^8$ . The steady state values are compared in Table 1. In the top panel of Table 1, the steady state Nusselt number for  $Ra_L = 10^5$  and  $Pr_f = 0.1$  obtained from present NDLBM is compared to the SIMPLE method solution of [29] and projection method solution of [2]. Then the steady state Nusselt number from the present NDLBM is compared to results of De vahl Davis [28] and Fuentes [30] for  $Ra$  from  $10^4$  to  $10^6$  with  $Pr_f = 0.71$ . The present NDLBM results for steady state Nusselt numbers agree very well with previous studies. In Fig. 2, for each  $Ra_L$ , a colored circle is located at the exact time point of  $Fo = 1/\sqrt{Ra_L}$ , i.e.  $\frac{t}{L/U} = \sqrt{Pr_f}$ , when natural convection begins and the Nusselt number begins to deviate from that for conduction. The good agreement of the initial  $Fo$  for each simulated case with  $1/\sqrt{Ra_L}$  also validates the present code for transient fluid flow and heat transfer.

A problem for melting of PCM in a square enclosure proposed by Mencinger [6] was used to validate the present code for melting. To solve Mencinger's problem, we set  $T_{ref} = T_{low} = T_m$ , and  $\Delta T = T_{high} - T_{low}$ . Hence  $T_{high}^* = 1$  and  $T_m^* = T_{low}^* = 0$ . The initial porosity of the melting procedure is set to zero to simulate pure solid. Three cases with dimensionless governing parameters  $(Pr_f, Pr_s, Ra_L, Ste) = (0.02, 0.02, 2.5 \times 10^4, 0.01)$ ,  $(0.02, 0.02, 2.5 \times 10^5, 0.01)$ , and  $(50, 50, 10^8, 10)$  were simulated. Fig. 3 compares contour plots of transient streamlines with porosity and isotherms of those obtained with the SIMPLE method by Mencinger [6] and those obtained by the

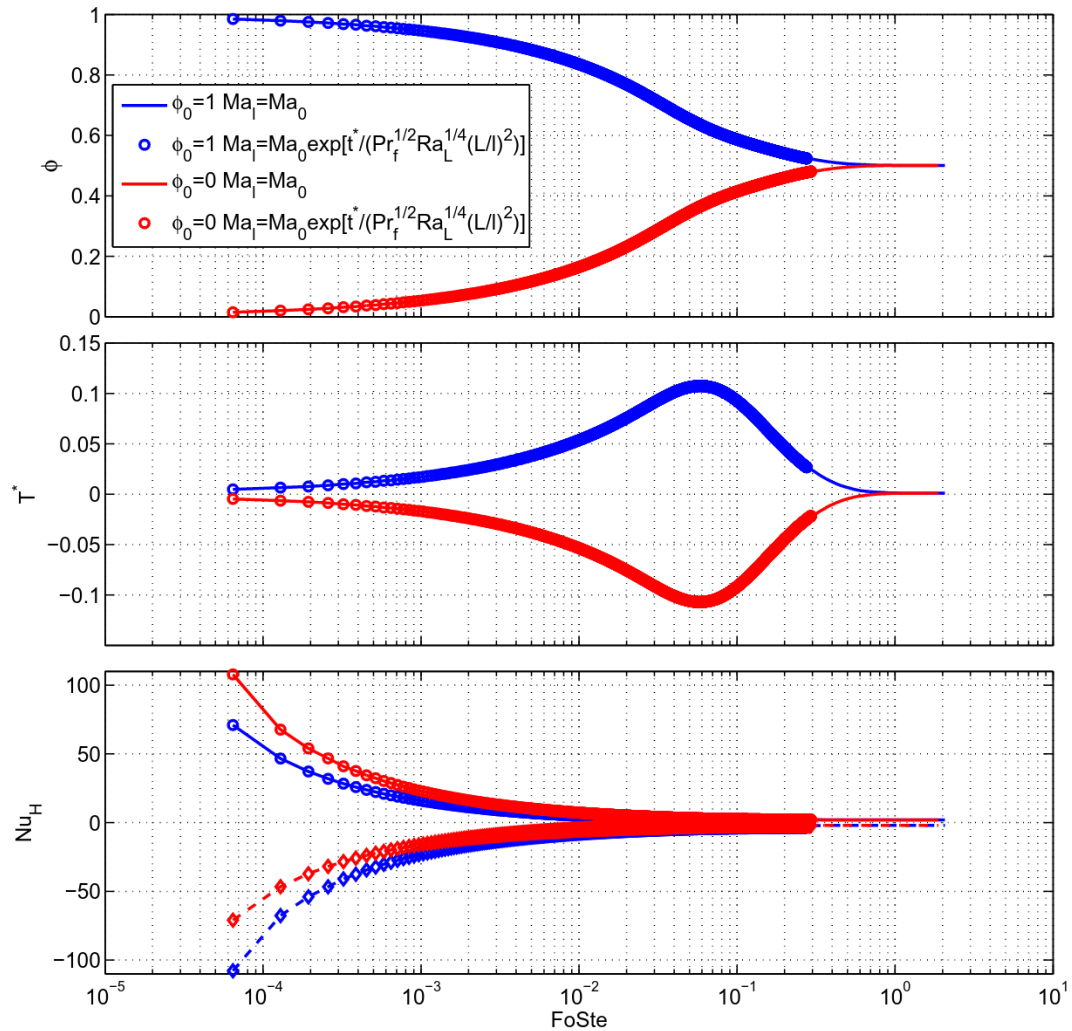


**Fig. 5.** Comparison of transient enclosure averaged porosity, dimensionless temperature, and  $Nu_H$  on the hot and cold walls for variable time steps using  $Ma_t$  in Eq. (43) (pen symbols) and fixed time steps  $Ma_t = Ma_0 = \sqrt{L/t}$  (solid lines) for  $(Pr_f, Pr_s, Ra_L, Ste) = (1, 1, 10^3, 1)$ . Solidification is indicated in blue and melting in red. (For interpretation of the references to colour in this figure caption, the reader is referred to the web version of this article.)

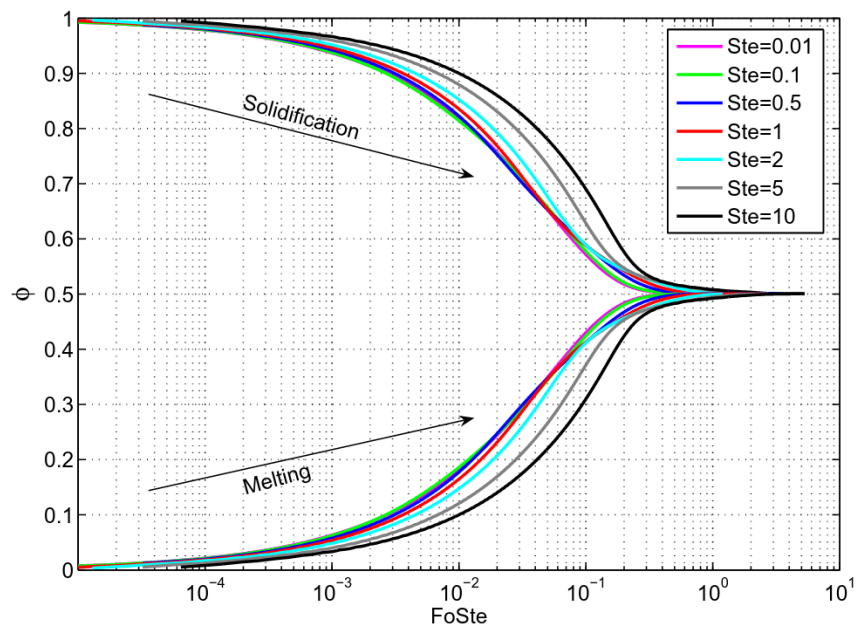


**Fig. 6.** Transient porosity for both solidification and melting for  $Ra_L = 10^3$  with  $Ste = 0.01, 0.1, 0.5, 1, 2, 5$ , and  $10$ .

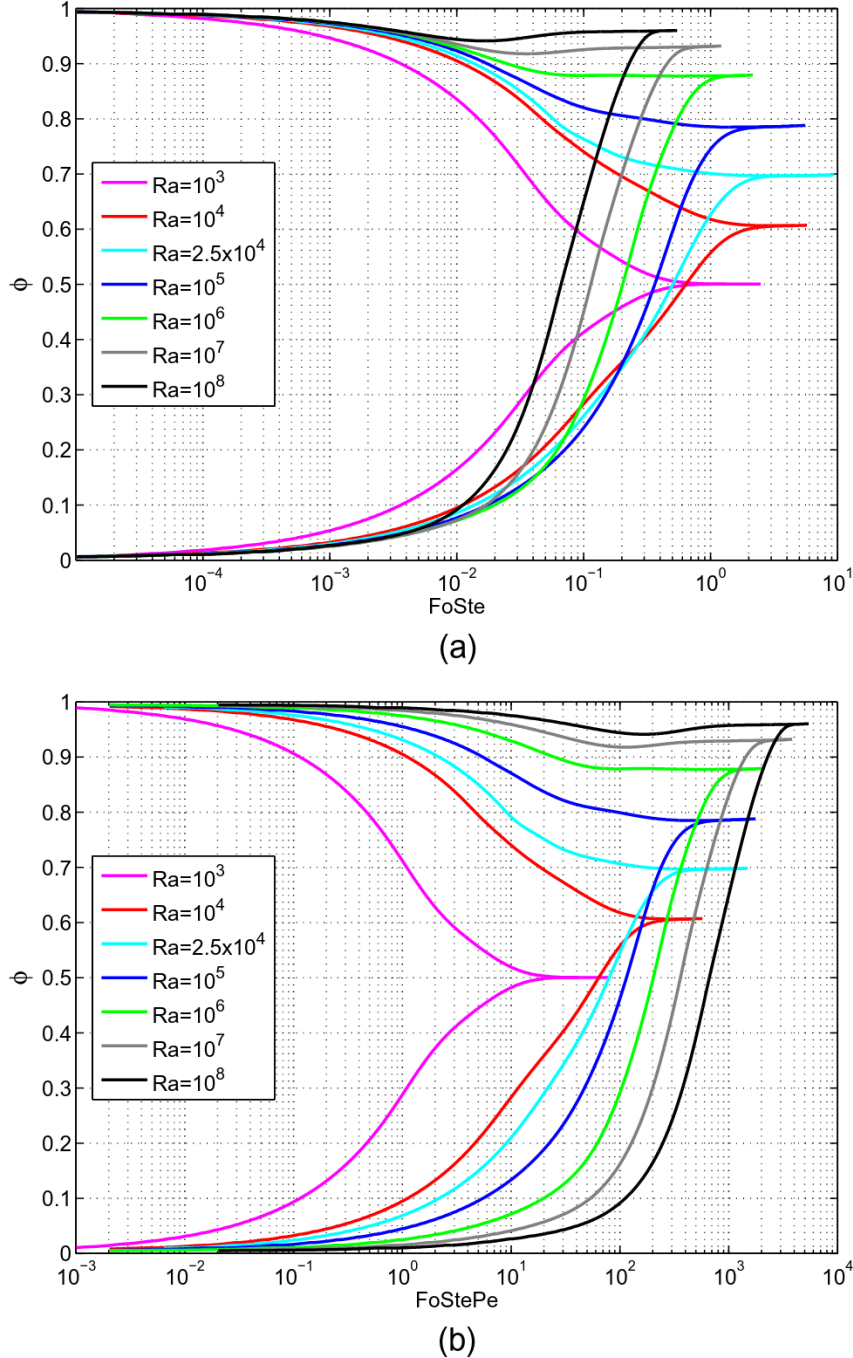


**Fig. 7.** Transient enclosure averaged porosity for various  $Ra_L$ : (a) Transient enclosure averaged porosity in time scale of  $FoSte$  and (b) Transient enclosure averaged porosity in time scale of  $FoStePe$ .

NDLBM. There is excellent agreement of the flow and heat transfer patterns from the three cases. Both models capture the effect of changes in  $Ra_L$  on the flow pattern. The isotherms are also similar; however the NDLBM method more accurately models the interface. As shown in Fig. 3(a), the NDLBM results of contour plots of streamlines are blue colored lines, while the gray colored lines are contour plots of porosity. With the new method, the interface is not an infinite thin line but a mixture zone. The thicknesses of transient mixture zone are 1.23% $L$  for  $Ra_L = 2.5 \times 10^4$ , 1.16% $L$  for  $Ra_L = 2.5 \times 10^5$ , and 0.87% $L$  for  $Ra_L = 10^8$ . The thickness of the mixture zone increases as  $Ra_L$  is decreased. The melting zone positions for the equilibrium state have been compared with experimental

study of Beckermann and Viskanta [19] and are plotted in Fig. 4. Experimental measured results of Beckermann and Viskanta [19] are represented by open black symbols and the melting zone positions of present NDLBM simulations are indicated by solid lines. For the measured four cases of Beckermann and Viskanta [19],  $Pr_f = Pr_s = 0.0208$ , the thermal diffusivity ratio of solid over fluid equals 1.105, and the density ratio of solid over fluid is 0.969. The black circles, diamonds, triangles, and squares represent the cases of  $(Ra_L, Ste, T_{PCM}^*) = (3.275 \times 10^5, 5.074 \times 10^{-2}, -0.36)$ ,  $(3.275 \times 10^5, 5.074 \times 10^{-2}, +0.32)$ ,  $(1.673 \times 10^5, 2.592 \times 10^{-2}, +0.48)$ , and  $(4.877 \times 10^5, 7.557 \times 10^{-2}, -0.0133)$ , respectively. The excellent agreement of the melting zone positions of present

simulations and the measurement of Beckermann and Viskanta [19] are additional validation of the present NDLBM code.

### 3.2. Melting and solidification of PCM in a square enclosure

To model the problem where melting and solidification reach the same equilibrium state, we choose  $T_{ref} = T_m$ . Hence  $T_{high}^* = 1$ ,  $T_{low}^* = -1$ , and  $T_0^* = T_m^* = 0$  for both melting and solidification.

#### 3.2.1. Validation of variable timestep method with transient $Ma_e$

First, cases with  $Pr_f = Pr_s = 1$ ,  $Ra_L = 10^3$ , and  $Ste = 1.0$ , are simulated to validate the variable time step scheme with transient  $Ma_e$  of Eq. (43). Fig. 5 shows the transient spatially averaged porosity, dimensionless temperature, and Nusselt number on the hot and cold walls for both solidification and melting. The blue lines and symbols represent solidification, and the red lines and symbols represent melting. The lines represent the fixed timestep simulation results, and circles or diamonds represent the variable timestep simulation results. In the bottom plot, solid lines and circles represent  $Nu_H$  on the hot wall and dashed lines and diamonds represent  $Nu_C$  on the cold wall. The results show that the present time adjustable scheme agrees with the results obtained from fixed time steps. For the case presented in Fig. 5, the CPU time of the variable timestep method is about 60% comparing to the fixed timestep method. Fig. 5 also shows that the same equilibrium state is reached for both melting and solidification with the same spatially averaged porosity.

#### 3.2.2. Effect of $Ste$

The value of  $Ste$  affects the speed of phase change. Fig. 6 shows that when  $Ste \leq 1$ , the transient enclosure averaged porosity versus  $FoSte$  are nearly identical. When  $Ste > 1$ , the transient enclosure averaged porosity lags behind those of  $Ste \leq 1$  and the lag increases with increasing  $Ste$ . When  $Ste < 1$ , the heat transfer limi-

tation is the melting/solidification. When  $Ste > 1$  the heat transfer limitation is the convection, so the transient enclosure averaged porosity lines separate. For all  $Ste$ , both melting and solidification reach the same equilibrium state as time goes to infinity, when  $Pr_f$ ,  $Pr_s$ , and  $Ra_L$  are fixed.

#### 3.2.3. Effect of $Ra_L$

The transient enclosure averaged porosities for  $Ste = 1$ ,  $Pr_f = Pr_s = 1$  and  $Ra_L$  from  $10^3$  to  $10^8$  are shown in Fig. 7. Fig. 7(a) is plotted versus the time scale  $FoSte$ , while Fig. 7(b) is plotted versus the time scale  $FoStePe$ , which is linear with respect to actual time. Both plots show the equilibrium state enclosure averaged porosity  $\phi_{equ}$  increases with increasing  $Ra_L$ . When  $Ra_L$  is  $10^3$ ,  $\phi_{equ} \approx 0.5$ , which means the equilibrium interface is in the middle of the enclosure and conduction dominates heat transfer. The equilibrium interface position shifts towards the cold wall with increasing  $Ra_L$ . For example, for  $Ra_L = 10^5$ ,  $\phi_{equ} \approx 0.8$ . Fig. 7(b) shows the real time to reach the equilibrium state increases with  $Ra_L$ .

The higher values of the transient Nusselt numbers (on the hot wall for the melting and on the cold wall for solidification) for various  $Ra_L$  are plotted in Fig. 8. Transient Nusselt numbers increase with increasing  $Ra_L$  and decrease with time. The step changes in the transient Nusselt numbers have been also observed by other fixed timestep simulations for melting at  $Ra = 2.5 \times 10^4$  and  $2.5 \times 10^5$  [6,14]. However due to the limited simulation time and  $Ra_L$  range, the prior work did not give the full map of the transient Nusselt numbers. The melting and solidification curves are less symmetrical at higher  $Ra_L$ . The asymmetry is consistent with the differences in the interface position at the equilibrium state (see Fig 7). The time for the melting procedure to reach the equilibrium state is longer than the solidification procedure at  $Ra_L = 10^8$ .

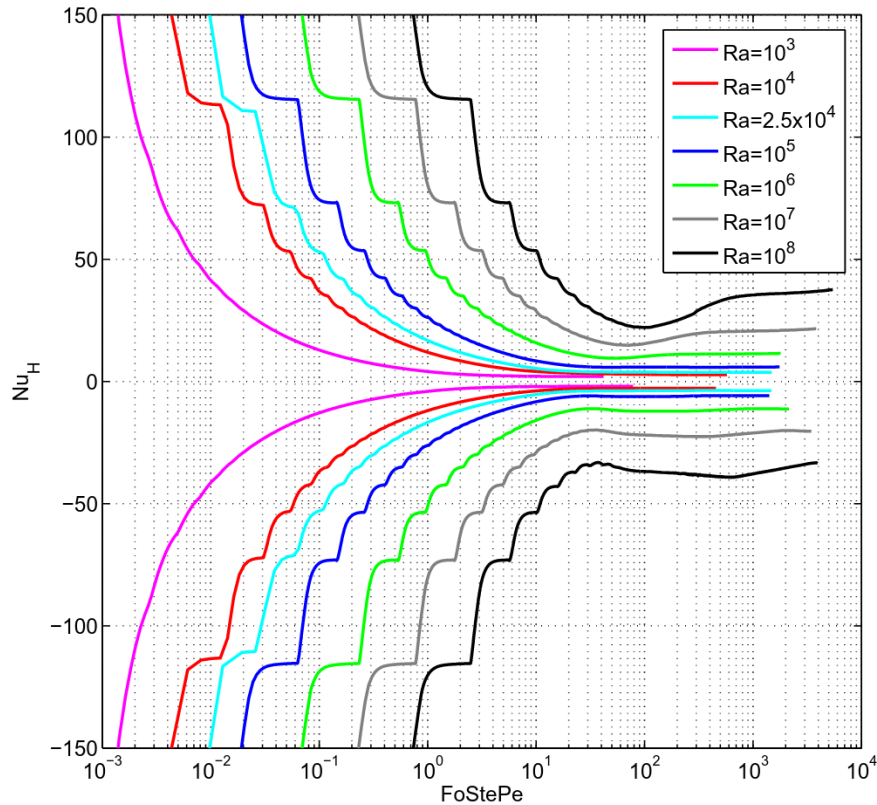


**Fig. 8.** The high values of the transient Nusselt numbers (on the hot wall for the melting and on the cold wall for solidification) for various  $Ra_L$ .

Contour plots of the dimensionless streamlines with porosity and isotherms are shown in Fig. 9 for  $10^3 \leq Ra_L \leq 10^8$ . The equilibrium state streamlines and isotherms change gradually with increasing  $Ra_L$ . For  $Ra_L = 10^3$ , the isotherms are almost vertical and parallel. The interface zone of the liquid and solid, denoted by dark gray lines, is almost vertical, and the equilibrium state streamlines have regular shape in the left half of the enclosure where the PCM has melted. Hence at  $Ra_L = 10^3$ , natural convection is weak, and heat transfer is dominated by conduction. At  $Ra_L = 10^4$  (Fig. 9(b)) the equilibrium state isotherms in the melt are no longer vertical because natural convection is stronger. The streamlines in the fluid stretch towards the solid liquid interface with a tilted angle of about  $68^\circ$  at the midheight. At  $Ra_L = 10^5$  (Fig. 9(c)) the isotherms and streamlines flatten in the fluid due to thermal stratification. Also a second recirculation appears in the center region of the fluid zone. At  $Ra_L = 10^6$  (Fig. 9(d)) the recirculations are stronger and have moved away from the interface toward the hot wall. For the equilibrium state, temperature and velocity overshoot within the boundary layer near the hot wall and the interface in  $+y$  and  $-y$  directions respectively. At  $Ra_L = 10^7$  (Fig. 9(e)) the size of the two recirculation cells near the hot wall and the interface shrink due to a thinning boundary layer. At  $Ra_L = 10^8$  (Fig. 9(f)) the recirculations almost disappear. For all  $Ra_L$ , melting and solidification reach the same equilibrium state, and the changes in the equilibrium state streamlines and isotherms with  $Ra_L$  are nearly identical.

However, the progression of the flow for melting and solidification differ. Fig. 10 shows contour plots of the transient dimensionless streamlines with porosity and dimensionless isotherms for  $Ste = 0.01$ ,  $Pr_f = Pr_s = 0.02$ , and  $Ra_L$  from  $2.5 \times 10^3$  to  $10^7$ . Increasing  $Ra_L$  increases the number but decreases the size of the thermal plumes and flow recirculations near the boundaries before the enclosure reaches the equilibrium state. For lower  $Ra_L = 2.5 \times 10^3$  when heat conduction dominates, the interface thickness of solidification at  $FoSte = 0.03$  is as large as  $2.57\%L$ . Also the thickness of the interface zone increases with the PCM solid heat conductivity and decreases with PCM latent heat.

### 3.2.4. Effects of $Pr_f$ and $Pr_s$

The transient enclosure averaged porosity for melting and solidification with  $Ste = 1$ ,  $Ra_L = 2.5 \times 10^4$ , and  $Pr_f$  and  $Pr_s$  from 0.1 to 10 are plotted in Fig. 11. Each type of line represents a set of melting and solidification with the same set of governing parameters. The lines starting at  $\phi = 0$  represent melting, and the lines starting at  $\phi = 1$  represent solidification. They merge into the same equilibrium state value of  $\phi_{equ}$ . Fig. 11(a) shows the transient heat transfer for melting and solidification is similar when  $Pr_f = Pr_s$  in time scale of  $FoSte$ . When other parameters are fixed,  $\phi_{equ(Pr_s < Pr_f)} < \phi_{equ(Pr_s = Pr_f)} < \phi_{equ(Pr_s > Pr_f)}$ . The five values of  $\phi_{equ} \approx 0.015, 0.1, 0.7, 0.96$ , and 0.99 from bottom to top correspond to  $Pr_s/Pr_f = 0.01, 0.1, 1, 10$ , and 100 respectively. So  $\phi_{equ}$  increases with  $Pr_s/Pr_f = \alpha_f/\alpha_s$ .

From Fig. 11(b), we can see that when other parameters are fixed, the time to reach equilibrium state  $t_{equ}$  changes with  $Pr_f$  and  $Pr_s$ . The values of  $\log(FoStePe)$  corresponding to  $t_{equ}$  are listed in Table 2. From Table 2, we can see that for fixed  $Pr_f$ , when  $Pr_f < 1$ ,  $t_{equ}$  decreases with  $Pr_s$ , and when  $Pr_f > 1$ ,  $t_{equ}$  increases with  $Pr_s$ . When  $Pr_f = 1$ ,  $t_{equ}$  increases with  $Pr_s$  for  $Pr_s \leq 1$  and decreases with  $Pr_s$  for  $Pr_s \geq 1$ . The trends are the same for fixed  $Pr_s$ .  $Pr_f$  or  $Pr_s$  equal to 1 represents the critical value of the relative

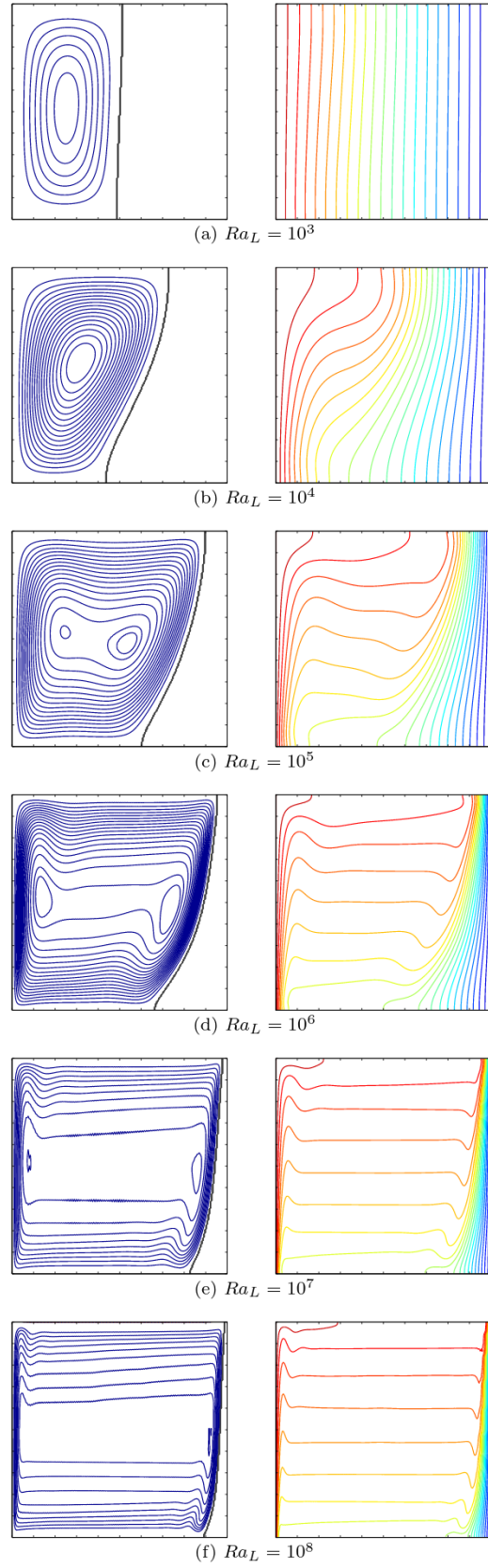


**Fig. 9.** Contour plots of equilibrium state dimensionless streamlines with porosity (left) and dimensionless isotherms (right) at equilibrium state for  $10^3 \leq Ra_L \leq 10^8$ .

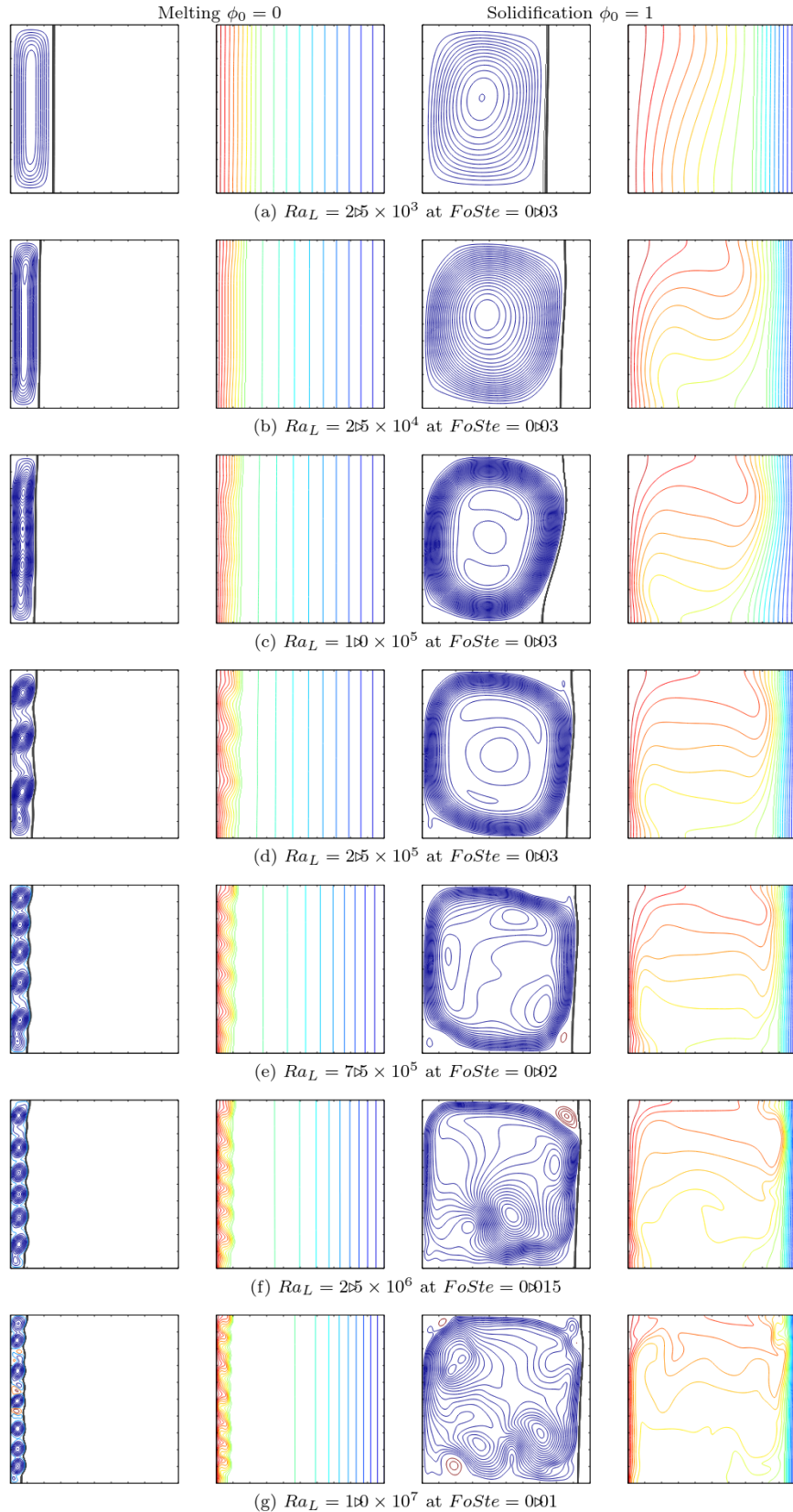


**Fig. 10.** Contour plots of transient dimensionless streamlines with porosity (left) and dimensionless isotherms (right) for  $Ste = 0.1$ ,  $Pr_f = Pr_s = 0.02$ , and  $Ra_L$  from  $2.5 \times 10^3$  to  $1.0 \times 10^7$ .

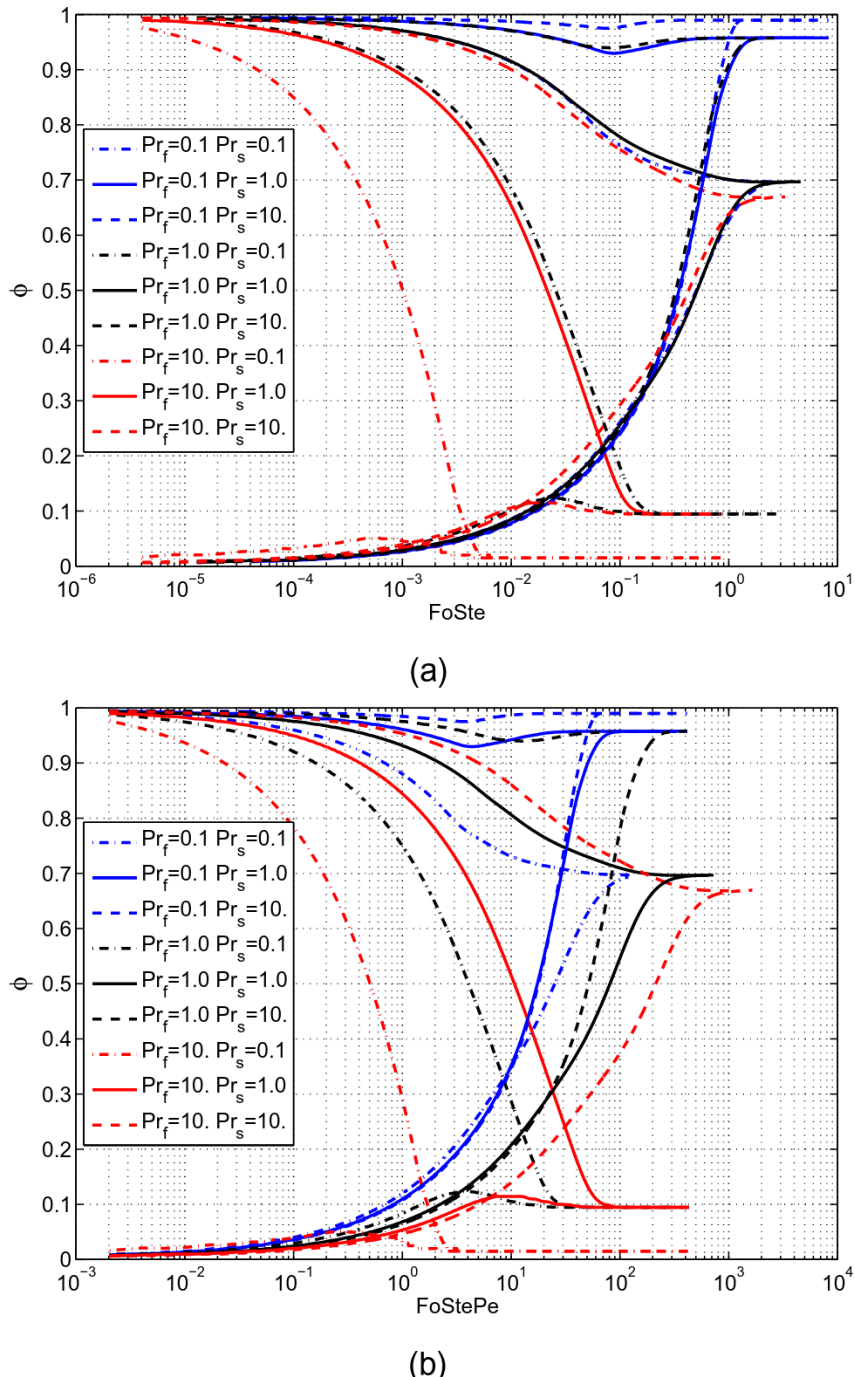


**Fig. 11.** Transient enclosure averaged porosity for  $Ste = 1$  and  $Ra_L = 2.5 \times 10^4$  with various  $Pr_f$  and  $Pr_s$ .

#### 4. Conclusion

A new mesoscopic scale time step adjustable NDLBM for solid-liquid phase change has been developed using scaling analysis based on the mesoscopic length and velocity scales. One of the benefits of the approach is time steps can be adjusted independent of mesh size by changing the transient mesoscopic Mach number. The code was validated by comparing the transient Nusselt numbers, isotherms, streamlines, melting fraction, and the transient interfaces between the fluid and solid with previous studies of natural convection in a square enclosure with and without PCM. A benchmark problem for melting and solidification of PCM in a square enclosure with natural convection starting from the melting

**Table 2**

The values of  $\log(FoStePe)$  at  $t_{equ}$  for  $Ste = 1$  and  $Ra_L = 2.5 \times 10^4$ .

	$Pr_f = 0.1$	$Pr_f = 1$	$Pr_f = 10$
$Pr_s = 0.1$	2.09	1.60	0.50
$Pr_s = 1$	2.07	2.75	2.02
$Pr_s = 10$	1.82	2.51	3.10

strength of the momentum diffusivity, thermal diffusivity of the fluid, and thermal diffusivity of the solid. At this critical value the heat transfer bottleneck changes among convection of the fluid, conduction of the fluid, and conduction of the solid.

temperature is proposed to obtain the same equilibrium state for both melting and solidification only with different initial porosity.

The full maps of the transient and equilibrium state porosity, streamlines and isotherms for both melting and solidification are given based on the key dimensionless governing parameters obtained from the scaling of governing equations. When  $Ste \leq 1$ , heat transfer is limited by the latent heat phase change, so the transient enclosure averaged porosities versus  $FoSte$  are almost overlapping. For  $Ste > 1$ , heat transfer is limited by natural convection, so the  $Ra_L$  affects both equilibrium and transient flow and heat transfer. The thicknesses of fluid and thermal boundary decrease with  $Ra_L$ , while  $\phi_{equ}$  increases with increasing  $Ra_L$ . Also increasing  $Ra_L$  will increase the number and decrease the size of the thermal plumes and flow recirculations near the boundaries in the transient procedures before they reach the equilibrium state. The time to reach the equilibrium state  $t_{equ}$  is compared, and the change of the heat transfer is discussed for various  $Pr_f$  and  $Pr_s$ . When other parameters are fixed,  $\phi_{equ}$  increases with  $Pr_s/Pr_f = \alpha_f/\alpha_s$ . Also  $Pr_f = 1$  or  $Pr_s = 1$ , represents the critical value of the relative strength of the momentum diffusivity, thermal diffusivity of the fluid, and thermal diffusivity of the solid. At this critical value the heat transfer bottleneck changes among convection of the fluid, conduction of the fluid, and conduction of the solid.

## Acknowledgments

We thank Prof. Frank Kulacki, University of Minnesota for suggesting this problem to us. Yan Su's study was supported by Solar Energy Lab of University of Macau with projects FDCT/060/2014/A2, FDCT/103/2014/SB, and MYRG2014-00014-FST. Also thanks the University of Minnesota Supercomputing Institute and High Performance Computing Cluster of Information and Communication Technology Office of the University of Macau.

## References

- [1] M. Eshraghi, S. Felicelli, An implicit lattice boltzmann model for heat conduction with phase change, *Int. J. Heat Mass Transfer* 55 (2012) 2420–2428.
- [2] Y. Su, J.H. Davidson, Multi-zone porous enclosure model of thermal/fluid processes during discharge of an inclined rectangular storage vessel via an immersed heat exchanger, *ASME J. Solar Energy Eng.* 129 (2007) 449–457.
- [3] M. Kamali, J. Gillissen, H. Akker, Lattice-boltzmann-based two-phase thermal model for simulating phase change, *Phys. Rev. E* 88 (3) (2013). 033302 (8).
- [4] J. Fuentes, F. Kuznik, K. Johannes, J. Virgone, Development and validation of a new LBM-MRT hybrid model with enthalpy formulation for melting with natural convection, *Phys. Lett. A* 378 (2014) 374–381.
- [5] A. Horibe, H. Jang, N. Haruki, Y. Sano, H. Kanbara, K. Takahashi, Melting and solidification heat transfer characteristics of phase change material in a latent heat storage vessel: effect of perforated partition plate, *Int. J. Heat Mass Transfer* 82 (2015) 259–266.
- [6] J. Mencinger, Numerical simulation of melting in two-dimensional enclosure using adaptive grid, *J. Comput. Phys.* 198 (2004) 243–264.
- [7] Y. Guo, R. Bennacer, S. Shen, D.E. Ameziani, M. Bouzidi, Simulation of mixed convection in slender rectangular enclosure with lattice boltzmann method, *Int. J. Numer. Methods Heat Fluid Flow* 20 (2010) 130–148.
- [8] B. Mondal, S.C. Mishra, Simulation of natural convection in the presence of volumetric radiation using the lattice Boltzmann Method, *Numer. Heat Transfer, Part A* 55 (2009) 18–41.
- [9] F.H. Lai, Y.T. Yang, Lattice Boltzmann simulation of natural convection heat transfer of Al2O3/water nanofluids in a square enclosure, *Int. J. Therm. Sci.* 50 (2011) 1930–1941.
- [10] A.A. Mehrizi, M. Farhadi, H.H. Afrooz, K. Sedighi, A.A.R. Darz, Mixed convection heat transfer in a ventilated enclosure with hot obstacle: effect of nanofluid and outlet port location, *Int. Commun. Heat Mass Transfer* 39 (2012) 1000–1008.
- [11] A. Tarokh, A.A. Mohamad, L. Jiang, Simulation of conjugate heat transfer using the lattice Boltzmann method, *Numer. Heat Transfer, Part A* 63 (2013) 159–178.
- [12] B. Mondal, S.C. Mishra, Simulation of natural convection in the presence of volumetric radiation using the lattice Boltzmann Method, *Numer. Heat Transfer, Part A* 55 (2009) 18–41.
- [13] A. Sakurai, S.C. Mishra, S. Maruyama, Radiation element method coupled with the lattice Boltzmann method applied to the analysis of transient conduction and radiation heat transfer problem with heat generation in a participating medium, *Numer. Heat Transfer, Part A* 57 (2010) 346–368.
- [14] F. Huang, H. Wu, P. Cheng, A new lattice Boltzmann model for solid-liquid phase change, *Int. J. Heat Mass Transfer* 59 (2013) 295–301.
- [15] S.F. Hosseini-zadeha, A.A. Rabienataj Darzib, F.L. Tanc, Numerical investigations of unconstrained melting of nano-enhanced phase change material (NEPCM) inside a spherical container, *Int. J. Therm. Sci.* 51 (2012) 77–83.
- [16] D. Noble, J. Torczynski, A lattice-Boltzmann method for partially saturated computational cells, *Int. J. Modern Phys. C* 9 (1998) 1189–1202.
- [17] Y. Su, F.A. Kulacki, J.H. Davidson, Experimental and numerical investigations on a solar tracking concentrated photovoltaic-thermal system with a novel non-dimensional lattice Boltzmann method, *Solar Energy* 107 (2014) 145–158.
- [18] Y. Su, J.H. Davidson, A non-dimensional lattice Boltzmann method for direct and porous medium model simulations of 240-tube bundle heat exchangers in a solar storage tank, *Int. J. Heat Mass Transfer* 85 (2015) 195–205.
- [19] C. Beckermann, R. Viskanta, Effect of solid subcooling on natural convection melting of a pure metal, *Trans. ASME J. Heat Transfer* 11 (1989) 416–424.
- [20] C. Beckermann, R. Viskanta, Natural convection solid/liquid phase change in porous media, *Int. J. Heat Mass Transfer* 31 (1988) 35–46.
- [21] Y. Su, J.H. Davidson, F.A. Kulacki, Numerical study on mixed convection from a constant wall temperature circular cylinder in zero-mean velocity oscillating cooling flows, *Int. J. Heat Fluid Flow* 44 (2013) 95–107.
- [22] X. He, L.S. Luo, Theory of the lattice Boltzmann: from the Boltzmann equation to the lattice Boltzmann equation, *Phys. Rev. E* 56 (1997) 6811–6817.
- [23] P.J. Dellar, Incompressible limits of lattice Boltzmann equations using multiple relaxation times, *J. Comput. Phys.* 190 (2003) 351–370.
- [24] Y. Su, J.H. Davidson, Natural convective flow and heat transfer in a collector storage with an immersed heat exchanger: numerical study, *ASME J. Solar Energy Eng.* 127 (2005) 324–332.
- [25] T. Inamuro, M. Yoshino, F. Ogino, A non-slip boundary condition for lattice Boltzmann simulations, *Phys. Fluids* 7 (1995) 2928–2930.
- [26] Q. Zou, X. He, On pressure and velocity boundary conditions for the lattice Boltzmann B model, *Phys. Fluids* 9 (1997) 1591–1597.
- [27] C.H. Liu, K.H. Lin, H.C. Mai, C.A. Lin, Thermal boundary conditions for thermal lattice Boltzmann simulation, *Comput. Math. Appl.* 59 (2010) 2178–2193.
- [28] G. De Vahl Davis, Natural convection of air in a square enclosure: a benchmark numerical solution, *Int. J. Numer. Methods Fluids* 3 (1983) 249–254.
- [29] J.H. Ferziger, M. Peric, Solution of the Navier–Stokes equations, *Computational Methods for Fluid Dynamics*, Hamburg, Germany, 1999, pp. 206–208.
- [30] J.M. Fuentes, K. Johannes, F. Kuznik, M. Cosnier, J. Virgone, Melting with convection and radiation in a participating phase change material, *Appl. Energy* 109 (2013) 454–461.

